PCCP

Accepted Manuscript

This is an *Accepted Manuscript*, which has been through the Royal Society of Chemistry peer review process and has been accepted for publication.

Accepted Manuscripts are published online shortly after acceptance, before technical editing, formatting and proof reading. Using this free service, authors can make their results available to the community, in citable form, before we publish the edited article. We will replace this *Accepted Manuscript* with the edited and formatted *Advance Article* as soon as it is available.

You can find more information about *Accepted Manuscripts* in the **Information for Authors**.

Journal Name

Physical Chemistry Chemical Physics

ARTICLE TYPE

Improved photocatalytic activity in RuO$_2$/ZnO nanoparticulate heterostructures due to inhomogeneous space charge effects

Tamez Uddin,[a] **Yohann Nicolas,**[a] **Céline Olivier,**[a] **Laurent Servant,**[a] **Thierry Toupance,*[a] Shunyi Li,**[b] **Andreas Klein**[b] **and Wolfram Jaegermann**[b]

New 2-6 wt% RuO$_2$/ZnO heterojunction nanocatalysts were synthesized by a straightforward two-step procedure. They were composed of a porous network of aggregated 25-nm wurtzite ZnO nanocrystallites modified with RuO$_2$ and showed enhanced light absorption in the visible region due to surface plasmon resonance. In order to investigate the energetic structure of the photocatalyst XPS
10 core line and valence band spectra of in-situ in UHV prepared heterointerfaces were compared to results obtained from the particles. The shift of Zn 2p$_{3/2}$ and O 1s core level spectra were determined to be at least 0.80 ± 0.05 eV for the in situ prepared heterojunction whereas it was found to be 0.40 ± 0.05 and 0.45 ± 0.05 eV, respectively in the photocatalysts. The different values were ascribed to the reduced size of the particles and the different measurability of band bending at the interface of the heterojunction RuO$_2$/ZnO compared to the nanoparticles. The RuO$_2$/ZnO photocatalysts showed higher photocatalytic activity and recyclability than pure ZnO for the degradation
15 of various dyes under UV light irradiation due to vectorial charge separation of photogenerated electrons and holes resulting from internal electric field, the ruthenium oxide acting as a quasi-metallic contact.

1 Introduction

Environmental issues along with the continuous increase of energy demands arising from the global population growth
20 require the development of advanced technologies for the production of green fuels. Also solutions for the efficient elimination of harmful pharmaceutical or organic pollutants are needed. In this context, semiconductor heterogeneous photocatalysis appeared to be a versatile concept for green
25 technology,[1,2] and was applied in a wide range of applications as hydrogen production, C-C bond formation, carbon dioxide remediation and depollution.[3] While anatase titanium dioxide (TiO$_2$) is the best understood semiconducting metal oxide prototype material for various photocatalytic applications,[4,5] zinc
30 oxide (ZnO) has been considered as a suitable alternative to titania owing to its nontoxicity, close band-gap energy (3.37 eV), high electron mobility (205-1000 cm^2.V^{-1}.s^{-1}),[6] large excitation binding energy (60 meV),[7] straightforward tailoring of the nanostructures and easy modification of the surface structure.[8,9]
35 Thus, ZnO showed better efficiency than TiO$_2$ in the photocatalytic decomposition of organic dyes either in organic or in aqueous media.[10,11,12,13] However, the fast recombination rate of photoinduced electron-hole pairs produced during photocatalytic processes has hampered the application of ZnO.
40 To circumvent these limitations, the design and modification of advanced ZnO photocatalysts with high sensitivity and reactivity have attracted much attention. One of the most promising ways for improving the photocatalytic performance consists in designing ZnO-based heterostructures or nanocomposites with
45 finely tuned electronic properties.[14,15,16,17] Thus, increased charge separation yields and extended energy range of photoexcitation

were achieved with ZnO-based coupled semiconductor systems such as ZnO-TiO$_2$,[18,19,20,21] ZnO-SnO$_2$,[22,23,24,25,26,27] or ZnO-WO$_3$,[28,29] that led to enhanced photocatalytic efficiencies. On the
50 other hand, loading noble metals on the surface of ZnO semiconductor also allowed for improving the photocatalytic activity of semiconductor via efficient trapping of the charge carriers.[30,31,32]

Among the metallic materials that can be combined with ZnO
55 for photocatalytic efficiency improvement, ruthenium(IV) oxide (RuO$_2$), that belongs to the family of transition metal oxides with rutile-like structure, represents an attractive candidate owing to its high chemical stability in both acidic and alkaline media, high conductivity,[33] excellent diffusion barrier properties and easy
60 processing as nanomaterials.[34,35] In particular, RuO$_2$ has an intrinsic submetallic property and its Fermi level EF is located in the partially filled Ru 4d state.[36,37] Thus, RuO$_2$-based nanomaterials were used for CO oxidation in sensors,[38] CO and CO$_2$ methanation,[39] HCl oxidation,[40] chlorine electrogeneration[41]
65 and water splitting.[42] Furthermore, combined in small amount with TiO$_2$, RuO$_2$ acts as an efficient hole and electron transfer catalyst[43] which was exploited in various photocatalytic reactions. [44,45,46,47] Considering the similar electronic properties of TiO$_2$ and ZnO, and the high work function of RuO$_2$,[48] situated in the band
70 gap above the valence band of ZnO, a suitable band alignment should be reached in RuO$_2$/ZnO heterostructures favoring charge separation and, as a result, high photocatalytic efficiencies. However, to the best of our knowledge, no effort has been devoted to develop RuO$_2$/ZnO nanocatalysts for improving the
75 photocatalytic performances of ZnO. In addition, the heterointerface of RuO$_2$/ZnO composites still remains largely unexplored.[49]

We hereafter describe a systematic study on the effect of RuO_2 modification of ZnO nanopowders on its photocatalytic activity along with a determination of the band alignment in RuO_2/ZnO nanocomposites. Nanosized ZnO particles were first prepared by homogeneous precipitation using urea as precipitating agent followed by calcination, and, then, RuO_2/ZnO systems were prepared by impregnating the ZnO in ruthenium (III) chloride hydrate ($RuCl_3.xH_2O$) solution followed by calcination in air. The photocatalytic activity and recycling ability of the resulting RuO_2/ZnO heterostructures were investigated by decomposition of both cationic (methylene blue (MB)) and anionic (methyl orange (MO)) dyes under UV irradiation and compared to those of ZnO and commercial TiO_2 (P25) nanopowders. The enhancement in photocatalytic activity due to the presence of RuO_2 is studied by characterization of the materials and optimization of the reaction conditions. To highlight the relationship between the electronic properties and the photocatalytic activity, Ultraviolet Photoelectron Spectroscopy (UPS) and X-ray Photoelectron Spectroscopy (XPS) studies allowed for determining the band alignment of the RuO_2/ZnO photocatalyst. The effective charge separation related to the semiconductor heterojunction is responsible for the enhanced photocatalytic properties of the RuO_2/ZnO photocatalysts.

2 Experimental method

2.1 Preparation of heterostructure photocatalysts

Starting chemicals were purchased from Aldrich or Acros Organics in analytical grade and used as received. ZnO nanoparticles were first prepared by a homogeneous precipitation method from a solution of zinc diacetate dihydrate using urea as a precipitant. In a typical procedure, 1.62 g (7.4 mmol) of $Zn(CH_3COO)_2.2H_2O$ was dissolved in 200 mL of deionized water containing 6 g (100 mmol) of urea. The solution was stirred at room temperature in a round bottomed flask until a homogeneous solution was obtained, and then further heated at a temperature of 90 °C for 4 h. Upon completion of the reaction, the white precipitate obtained was centrifuged at 5000 rpm for 10 min and washed with deionized water until neutral pH. After elimination of the supernatant, the resulting powder was dried at 110 °C overnight followed by calcination at 350 °C in air for 2 h yielding ZnO nanoparticles (0.5 g, yield: 70%) that are named pure ZnO. RuO_2/ZnO heterostructures were prepared in the second step using the impregnation method. In a typical procedure, a suitable amount of ruthenium (III) chloride hydrate ($RuCl_3.xH_2O$) was dissolved into 50 mL deionized water. ZnO nanopowder (0.3 g) was then dispersed into the solution and was vigorously stirred for 8 h. After evaporation of the solvent and drying in air at 110 °C overnight, annealing at 350 °C in air for 2 h gave desired RuO_2/ZnO photocatalysts (0.3 g). The content of RuO_2 in RuO_2/ZnO samples was tuned by changing the concentration of the ruthenium (III) chloride hydrate solution. The samples containing 2, 4, and 6wt% of RuO_2 were obtained by adding 0.0183, 0.0374 and 0.0573 g of ruthenium (III) chloride hydrate, respectively, to deionized water (50 mL). The resulting samples are hereafter named 2wt% RuO_2/ZnO, 4wt% RuO_2/ZnO, and 6wt% RuO_2/ ZnO nanocomposites.

2.2 Characterization methods

The Fourier Transform Infrared (FTIR) spectra were recorded in pressed KBr pellets on a Perkin-Elmer Spectrum 100 FTIR spectrophotometer. Raman studies were carried out in the solid state on a Labram 1B spectrometer using a red laser beam (632 nm). X-ray diffraction (XRD) studies were recorded on a Bruker AXS diffractometer (D2 PHASER A26-X1-A2B0D3A) using a Cu anode ($K\alpha$ radiation). A continuous scan mode was employed to collect 2θ data from 10-80° with a 0.1° sampling pitch and a 2° min^{-1} scan rate. The average crystallite size of the nanomaterials prepared was deduced from FWHM (full width at half maximum) according to Scherrer's formula (applied to the {101} reflection).[50] Nitrogen adsorption-desorption measurements were carried out with an ASAP2010 micromeritics equipment on samples degassed at 120 °C under vacuum. The specific surface areas (S_{BET}) were calculated by applying the BET (Brunauer-Emmett-Teller) equation between 0.1 and 0.3 relative pressures.[51] The nitrogen adsorption-desorption isotherms were measured at liquid nitrogen temperature (77 K) taken P/P_0 from 0 to 0.99. Pore size distributions were evaluated by the Barrett, Joyner, Halenda (BJH) model applied to the adsorption branch of the isotherms. HR-TEM images were recorded with JEOL JEM-2200FS microscopes after dispersing the powders in ethanol and coating a small droplet of the suspension on holey carbon (Cu) grid. UV-VIS diffuse reflectance spectra (DRS) of the samples were measured at room temperature in the wavelength range of 200-800 nm using an UV-VIS-NIR spectrometer (Lambda 900). Pure powdered $BaSO_4$ was used as a reference. The band gap energy (E_g) of the various samples prepared was deduced from their absorption spectra by using the following equation (Tauc relation), $\alpha(h\nu) = A(h\nu - E_g)^n$ where α, ν, E_g, A and n are the absorption coefficient, light frequency, band gap energy, a constant and a parameter depending on the nature of the semiconductor, respectively.[52] In the case of powdered materials, the absorption coefficient (α) can be estimated from the remission function, F(R), that can be written in terms of diffuse reflectance (R) of the sample according to the Kubelka-Munk theory:

$$\alpha / s = F(R) = \frac{(1-R)^2}{2R},$$

where s is the scattering coefficient.[53] Assuming that the scattering coefficient s is almost constant on the wavelength range investigated, the remission function F(R) appears proportional to the absorption coefficient (α). As ZnO is a direct band gap semiconductor, the optical band gap energies can be estimated from a plot of $[F(R)h\nu]^2$ as a function of $h\nu$. In the case of a direct transition (n = 1/2),[54] extrapolating the linear region of the above curve, to the abscissa yields the band gap energies (E_g) of the samples studied.

X-ray Photoelectron spectra of the photocatalysts were carried with a PHOIBOS 225 (Specs GmbH) spectrometer. Monochromatized X-ray ($K\alpha$: 1486.61 eV) from an Al anode was used for excitation. The spectrometer was referenced to the core level and valence band spectra of sputtered Au and Ag foils and a possible charging effect was inferred from the main component of the C 1s peak, associated with adventitious hydrocarbons with a binding energy of 284.8 eV as reference for

calibration. The base pressure in the sample during the measurements was less than 3×10^{-8} mbar. The energy band diagram of the RuO$_2$-ZnO heterostructure was determined by XPS using well-known procedures from the literature.[55,56,57]

Commercial ZnO single crystal substrates (alineason, Frankfurt, Germany) with the dimension $5 \times 5 \times 0.5$ mm^3 have been used for the interface experiments using the DAISY-MAT system equipped with a Physical Electronics 5700 photoelectron spectrometer also with monochromatized Al Kα radiation. Spectral calibration was performed as described above. The substrates were single-side epi-polished with Zn- and O-termination, respectively. Before introducing them into the UHV system, the substrates were cleaned with acetone in ultrasonic bath for 10 min and rinsed with isopropanol, ethanol, distilled water, and finally dried with N$_2$. Two pieces of ZnO substrates with different termination mounted on the same sample holder were annealed in 0.5 Pa O$_2$ at around 400 °C for 30 min in order to remove the residual hydrocarbon contaminations on the surface. Additional experiments have been performed with ZnO thin films deposited in situ by reactive DC sputter deposition onto conductive glass. The XPS measurements after the cleaning steps showed no traces of carbon. The deposition of RuO$_2$ has been carried out via reactive DC sputtering (P=10 W) at room temperature with a metallic Ruthenium target, having a purity of 99.99% and a diameter of 2 inch. A gas mixture of 7.5% O$_2$ and 92.5% Ar was used as sputter gas, which yields fully oxidized and highly conductive RuO$_2$ thin films.[48] The deposition rate of RuO$_2$ is about 3 nm/min determined by thickness measurements with a profilometer.

2.3 Photocatalytic experiments

The photocatalytic activities of the nanocomposites were evaluated in terms of degradation rate of methylene blue (MB) or methyl orange dye (MO) (Alfa Aesar, reagent grade, used as supplied) measured at room temperature under air. In each experiment, 0.1 g of photocatalyst was dispersed in 100 mL of MB or MO aqueous solution (10 mg/L) to obtain the concentration of the catalyst at 1.0 g/L. The experiments were performed in a Pyrex beaker illuminated with a 125 W high pressure mercury lamp (Philips, HPL-N 125 W/542 E27) emitting UV light (365 and 313 nm), positioned above the solution beaker. Prior to irradiation, the suspension was stirred in the dark for 30 min to reach adsorption/desorption equilibrium. The solutions were continuously stirred during the experiments. During the illumination process, 4 mL of the suspensions were collected at given irradiation time intervals, and then centrifuged (4000 rpm, 10 min) to separate the nanocomposite particles. The MB or MO concentration was determined by monitoring the wavelength of maximum absorption at λ_{max} = 664 nm for MB and at λ_{max} = 464 nm for MO observed by UV-Visible spectroscopy (Shimadzu UV-1650 pc spectrophotometer). A calibration plot based on Beer–Lambert's law was established by relating the absorbance to the concentration. In each case, blank experiments were also conducted with the catalysts in the absence of light and without the catalysts when the solution containing the dissolved dye was illuminated. For sake of comparison, the same experiments were carried out with commercial TiO$_2$ (Degussa, P-25) used as a photocatalytic standard. In some cases, repetitive
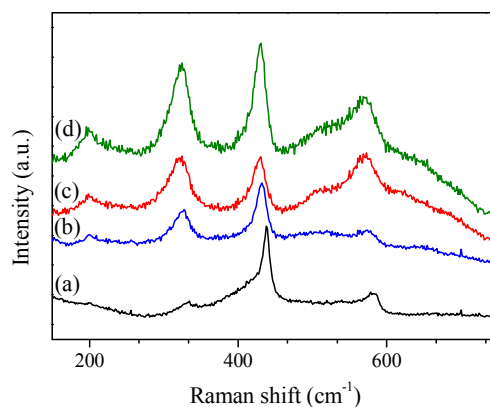

Fig. 1 Raman spectra of ZnO (a, black), 2wt% RuO$_2$/ZnO (b, blue), 4wt% RuO$_2$/ZnO (c, red) and 6wt% RuO$_2$/ZnO (d, olive) nanomaterials.

photodegradation of MB during four consecutive cycles was performed with 1.0 g/ L of catalyst at 10 mg/ L dye concentration After each cycle, the catalyst was washed with distilled water and a fresh solution of MB was added before each photocatalytic run.

3 Results and discussion

3.1 Synthesis and Characterization of nanocatalysts

A two-step procedure was set up to prepare RuO$_2$/ZnO nanocomposites. At first, nanosized ZnO particles were synthesized by the homogeneous precipitation method using zinc acetate and urea as the precursor and precipitating agent, respectively. Reaction of zinc acetate with urea at 90°C in aqueous media led to precipitation of Zn(OH)$_2$. The pH of the solution increased gradually due to the progressive decomposition of urea into NH$_3$ and CO$_2$, yielding the nucleation and growth of ill-crystallized nanosized particles (Fig. S1) which were calcined at 350 °C. Further impregnation of the resulting ZnO nanoparticles with a solution containing a suitable amount of ruthenium (III) chloride hydrate (RuCl$_3$.xH$_2$O) to include 2, 4 and 6 wt% of RuO$_2$ gave the 2 wt%, 4 wt% and 6 wt% RuO$_2$/ZnO nanocomposites after annealing in air at 350°C. Elimination of the undesirable organics and formation of metal oxide species upon calcination were checked by FTIR spectroscopy (Supporting information Fig. S2). Thus, irrespective of the RuO$_2$ content, the FTIR spectrum for each RuO$_2$/ZnO sample showed a broad absorption band centered at 3434 cm^{-1} assigned to the superposition of the stretching vibration bands of surface hydroxyl groups ν(O-H) or adsorbed water molecules along with a band at 1631 cm^{-1} attributed to bending vibration δ(O-H) of molecular water. Moreover, an intense absorption band was detected at 505 cm^{-1} assigned to the stretching vibration mode of Zn-O bonds in zinc oxides.[58,59] Then, Raman scattering spectroscopy provided further information concerning the nanocomposite nanostructure. The thermodynamically stable ZnO crystallite possesses a wurtzite (hexagonal) structure and belongs to the space group of C$_{6v}^4$ that leads to expect $A_1 + 2B_1 + E_1 + 2E_2$ optical phonon modes near the center of the Brillouin zone according to group theory. Among these optical phonon modes, A_1 and E_1 modes are both Raman and infra-red active. Moreover, these A_1 and E_1 modes are polar which split into

transverse optical (TO) and longitudinal optical (LO) phonons. E_2 mode consists of two modes of low- and high-frequency phonons which are Raman active only and B_1 modes are silent.[60,61,62] The bands in the Raman spectra can be entirely explained on the basis of published data for c-ZnO:[60,61,63] E_2 (low) at 101 cm^{-1}, E_2 (high) at 437 cm^{-1}, A_1 (TO) at 380 cm^{-1}, E_1 (TO) at 407 cm^{-1}, A_1 (LO) at 574 cm^{-1}, and E_1 (LO) at 583 cm^{-1}. The rest of the vibrations are usually labelled as second order vibrations.[64] On the other hand, RuO$_2$ has a rutile structure, which is tetragonal with two RuO$_2$ molecules per primitive unit cell. According to the factor group analysis, there are 15 optical modes of RuO$_2$, among which four modes are Raman active with symmetries A_{1g}, B_{1g}, B_{2g} and E_g.[65] The three major Raman features of a rutile single crystal RuO$_2$, namely the E_g, A_{1g}, and B_{2g} modes are located at 528, 646 and 716 cm^{-1}, respectively.[66] Figure 1 shows the Raman spectra of ZnO nanoparticles and RuO$_2$-ZnO nanocomposites.

The main dominant sharp peak labelled as E_2 at 438 cm^{-1} is known as Raman active phonon mode, which was characteristic of the wurtzite hexagonal phase of ZnO (Fig. 1-a). The very weak shoulder at 410 cm^{-1} in pure ZnO could be assigned to the mode of E_1(TO),[67] whereas the features at 205 cm^{-1} and 335 cm^{-1} are related to second order modes.[68,69,70] Finally, the first-order Raman peak at 585 cm^{-1} could be ascribed to the longitudinal optical (LO) phonons of E_1. On the other hand, the intensity of Raman peaks for RuO$_2$-ZnO nanocomposites was enhanced as compared to pure ZnO with increasing the amount of RuO$_2$ on the surface of ZnO nanocatalysts (Fig. 1b-d), namely for the first order LO phonon mode. In addition, the red shift of both E_2 mode and LO phonon could also be observed. This behaviour might be related to the presence of an electric field enhancing the
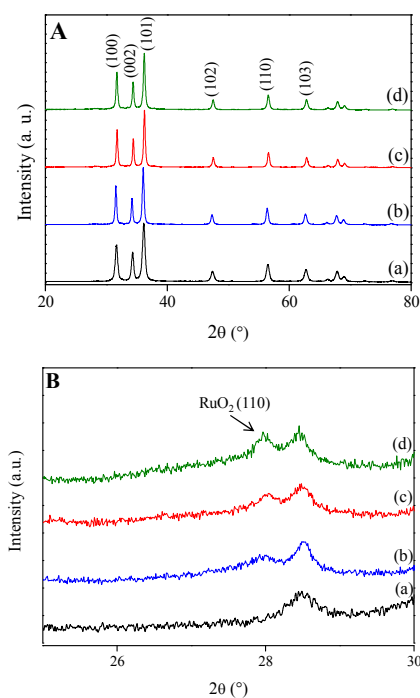

Fig. 2 XRD of ZnO (a, black), 2wt% RuO$_2$/ZnO (b, blue), 4wt% RuO$_2$/ZnO (c, red) and 6wt% RuO$_2$/ZnO (d, olive) nanomaterials: **A**: 2θ region of 20-80°. **B**: expand of the 2θ region of 26.5-30°.

scattering by Raman active optical phonons due to polarization by the field of the excitonic states. This scattering is proportional to the electric field and goes through a maximum. The transfer of
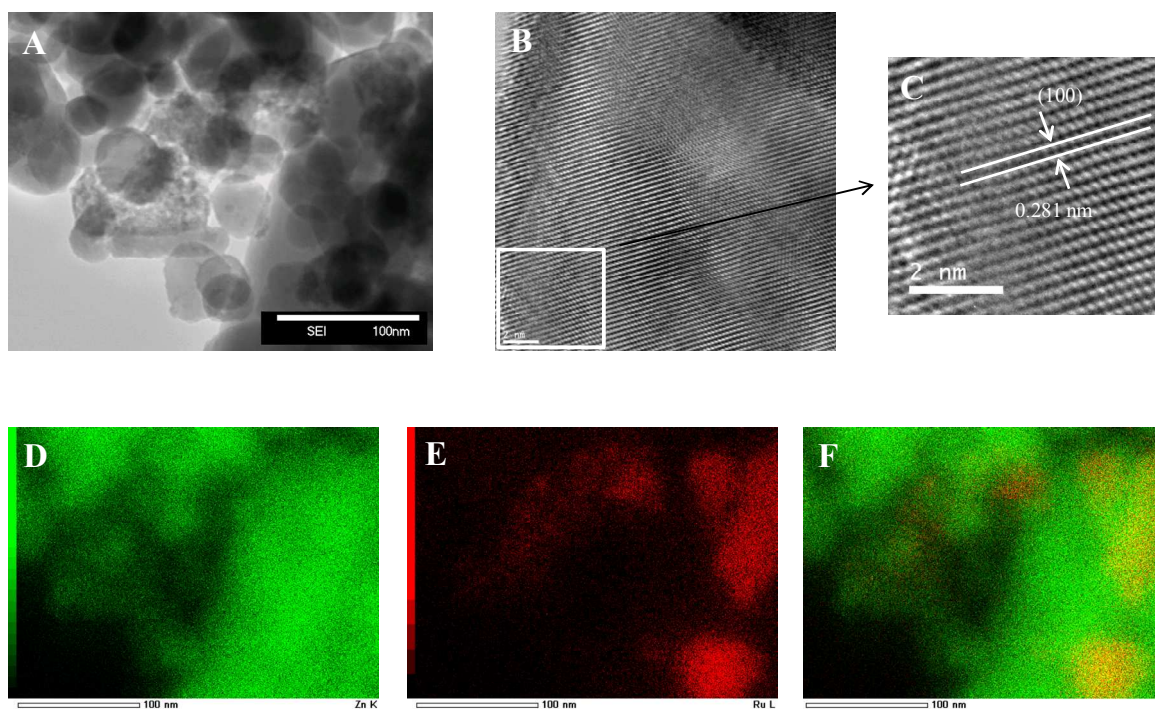

Fig.3 (A) STEM second electron image (SEI) of 4wt% RuO$_2$/ZnO; (B, C) HRTEM image of 4wt% RuO$_2$/ZnO; (D) EDX map of Zn K; (E) EDX map of Ru L; (F) EDX map of Zn K + Ru L.

Table 1 Nitrogen sorption porosimetry studies[a] and apparent rate constants for the degradation of MB[b] and MO[c] of ZnO and RuO₂/ZnO nanomaterials. [a] Surface areas were determined by BET, mean pore diameters by BJH theory (applied to the adsorption branch), and pore volumes by single-point analysis. [b] Kinetic data for the photocatalytic decomposition of methylene blue. [c] Kinetic data for the photocatalytic decomposition of methyl orange.

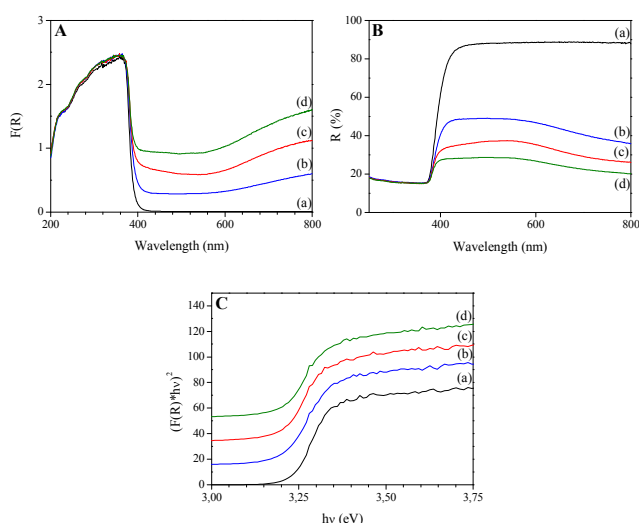| Photocatalyst	S_{BET} (m².g⁻¹)	Pore volume (cm³.g⁻¹)	Mean pore size (nm)	k_{app} (min⁻¹)	K_{norm} (g.m⁻².min⁻¹)
ZnO	31 ± 1	0.18 ± 0.02	23.0 ± 0.5	0.054[b] (0.024)[c]	1.74×10^{-3} [b] (0.77×10^{-3})[c]
2% RuO₂-ZnO	29 ± 1	0.14 ± 0.02	19.0 ± 0.5	0.071[b]	2.44×10^{-3} [b]
4% RuO₂-ZnO	25 ± 1	0.09 ± 0.02	14.0 ± 0.5	0.106[b] (0.035)[c]	4.24×10^{-3} [b] (1.40×10^{-3})[c]
6% RuO₂-ZnO	22 ± 1	0.08 ± 0.02	15.0 ± 0.5	0.066[b]	3.03×10^{-3} [b]
P25	47 ± 1.5	0.13 ± 0.01	11.5 ± 0.5	0.101[b] (0.033)[c]	2.14×10^{-3} [b] (0.7×10^{-3})[c]

Fig. 4 (A) UV-visible diffused absorption spectra; (B) UV-visible diffused reflectance spectra; (C) $(F(R) \ h\nu)^2$ versus hv plot for ZnO (a, black), 2wt% RuO₂/ZnO (b, blue), 4wt% RuO₂/ZnO (c, red) and 6wt% RuO₂/ZnO (d, olive) nanomaterials.

electrons from ZnO to RuO₂ leads to the formation of an interfacial electric field between ZnO and RuO₂ due to different work functions. This local electric field increases the electron-phonon coupling, which led to the enhancement of the Raman intensity of ZnO. Otherwise, more phonon modes of ZnO have been activated in RuO₂-ZnO nanocomposites compared to ZnO nanocatalysts.

The crystalline phases of the catalysts were further confirmed by using XRD analysis (Fig. 2). Irrespective of the RuO₂ content, the hexagonal wurtzite zinc oxide phase was clearly identifiable in the X-ray diffraction patterns of all the samples studied with main features at d (Å) values of {100}(2.815), {002} (2.603), {101} (2.476), {102} (1.911), {110} (1.625) and {103} (1.477) in well agreement with the reported data (JCPDS File No. 36-1451). Moreover, a close view in the 2θ range of 20-30° showed an extra peak at 2θ of 28° that could be indexed to RuO₂ (110) (Fig. 2B).[71] The intensity of RuO₂ peaks in the nanocomposite samples increased with the increase in the amount of RuO₂ content indicating the formation of RuO₂ along with ZnO. Moreover, the average crystal size of ZnO, deduced from line

broadening of the (101) diffraction peak according to the Scherrer formula, remained almost unchanged, i.e. 25 ± 1 nm, with increasing the RuO₂ content up to 6%.

To gain further insight of the microstructure, morphology and texture of the nanocomposites, TEM and N₂ sorption studies have been performed on the RuO₂/ZnO samples. At low magnification (Fig. 3A), the formation of nanocrystalline ZnO aggregates made of pseudo-spherical nanoparticles could be clearly evidenced, the average size of which are within the range of 25-30 nm which agrees well with the mean crystallite size deduced from XRD. The samples are therefore made of a network of aggregated nanoparticles. Furthermore, HRTEM images revealed the formation of well-crystallized nanoparticles with an interplanar distance of about 0.28 nm which is consistent with the lattice spacing of the (100) plane expected for the hexagonal wurtzite ZnO (Fig. 3B-C). Moreover, the formation of RuO₂ particles was assessed by EDX mapping (Fig. 3D-F), the measured weight percentage of RuO₂ being 3.75 wt% that is in close agreement with the expected one, i.e. 4 wt% (Fig. S3). As far as the N₂ sorption studies are concerned, each sample studied exhibited type-II N₂ sorption isotherm typical of a porous material including mainly large mesopores or macropores (Fig. S4). The pure ZnO catalyst showed a BET surface area of 31 m².g⁻¹ with mean pore diameter and total pore volume of 22.9 nm and 0.18 cm³/g, respectively. Upon loading with RuO₂, the BET surface area, mean pore diameter, and total pore volume slightly decreased with increasing the RuO₂ amount (Table 1). The decrease in BET surface area could result from the blocking of mesopore dimension when RuO₂ particles were deposited.

Finally, to determine their optical properties and estimate their energy band gap, the various photocatalysts prepared were investigated by Diffuse Reflectance UV-visible spectroscopy (DRS) (Fig. 4).[72] For each sample, a significant increase in the absorption at wavelengths shorter than 400 nm could be assigned to the intrinsic band gap absorption of ZnO (Fig. 4A). More interestingly, compared to pure ZnO, the RuO₂/ZnO nanocomposites showed an enhanced absorption in the visible region suggesting that these samples could be efficient for photocatalysis under visible light. In addition, the absorption increased with raising the RuO₂ content. This trend could be clarified in more details from UV-Vis diffused reflectance spectra

as shown in Fig. 4B. Thus, pure ZnO reflected about 89 % visible light and absorbed about 85 % UV light (Fig. 4Ba). In contrast, the reflectance of RuO_2/ZnO nanocomposites was lower than that of pure ZnO in the 400-800 nm wavelength range. The enhancement of visible-light absorption for the RuO_2/ZnO nanocomposites can be related to the fact that the incident photon frequency was resonant with the collective excitations of the conduction electrons of RuO_2 nanoparticles called localized surface plasmon resonance (LSPR).[49] Using the Kubelka-Munk model, the calculated band gap energy for pure ZnO was found to be 3.23 eV from the extrapolation of the corresponding plot which is consistent with that expected for nanoparticulate ZnO.[73] On the other hand, the estimated band gap energies decreased from 3.23 eV for pure ZnO to 3.14 eV, for 6 wt% RuO_2/ZnO (Fig. 4C).

3.2 Interface analysis

To highlight the elemental chemical composition of RuO_2/ZnO nanomaterials, X-ray photoelectron spectroscopy (XPS) studies were performed on pure ZnO and RuO_2/ZnO composites including various RuO_2 contents as well as in situ built-up RuO_2/ZnO heterointerfaces.

In the ex-situ analyzed samples, except for the C 1s peak located at 284.4 eV that may be assigned to adventitious carbonaceous species, solely zinc, ruthenium and oxygen related emissions were observed in the survey spectra of 4 wt% RuO_2/ZnO nanocatalyst whereas no Ru emission could be
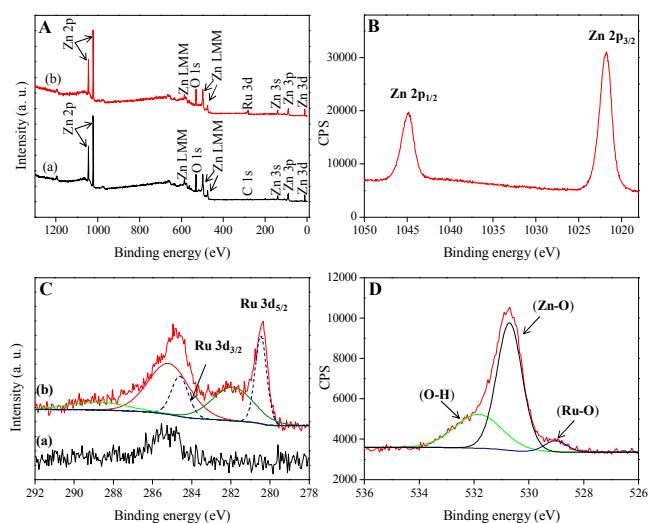

Fig. 5 (A) XPS survey spectra of ZnO (a, black) and 4 wt% RuO_2/ZnO (b, red). High-resolution spectra: (B) Zn 2p spectra of 4 wt% RuO_2/ZnO, (C) Ru 3d spectra of ZnO (a, black) and 4 wt% RuO_2/ZnO (b, red) and (D) O 1s spectra of 4 wt% RuO_2/ZnO.

detected in the spectrum of pure ZnO (Fig. 5A). As a result, the RuO_2/ZnO samples were only formed by Zn and Ru oxides which is consistent with the XRD and EDX results discussed above. The high resolution XPS spectrum for Zn 2p exhibited two symmetric
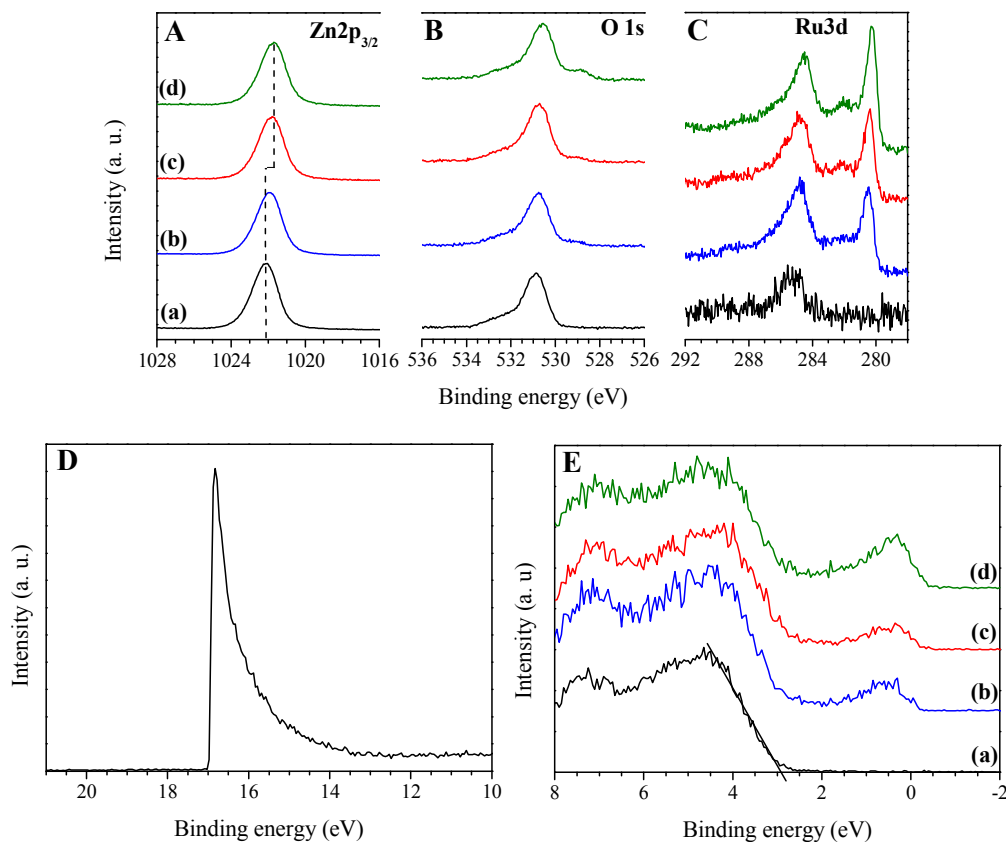

Fig. 6 Evolution of photoemission core level spectra of RuO_2/ZnO heterostructures as a function of RuO_2 content: (A) Zn $2p_{3/2}$; (B) O 1s; (C) Ru 3d; (D) UPS HE-I spectra of pure ZnO nanocatalyst; (E) XP valence band spectra of ZnO and RuO_2/ZnO with different content of RuO_2. ZnO (a, black), 2wt% RuO_2/ZnO (b, blue), 4wt% RuO_2/ZnO (c, red) and 6wt% RuO_2/ZnO (d, olive).
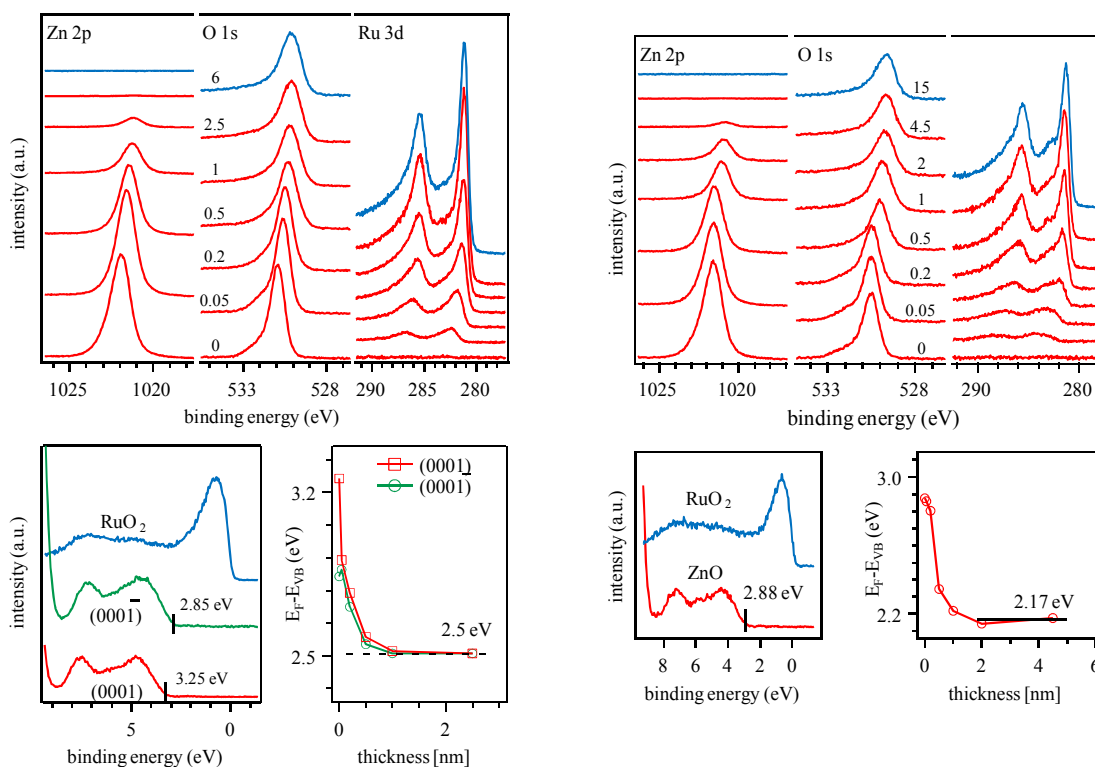
Fig. 7 Contact formation of single crystalline ZnO/RuO$_2$ interfaces (left) vs. polycrystalline interfaces (right) (top) X-ray photoelectron spectra recorded in the course of RuO$_2$ deposition onto a cleaned ZnO(0001) single crystal surface. The number indicates the RuO$_2$ thickness in nm. (bottom left) Valence band spectra of cleaned ZnO(0001) and ZnO(000$\bar{1}$) single crystal surfaces. The binding energy of the valence band maxima are indicated. (bottom right). Evolution of the valence band maxima as obtained from the Zn 2p core level binding energies in the course of simultaneous RuO$_2$ deposition onto both substrates.

peaks centred at 1021.83 and 1044.92 eV attributed to Zn 2p$_{3/2}$ and Zn 2p$_{1/2}$, respectively (Figure 5B). These data suggest that zinc exists as Zn^{2+} oxidation state in the composite samples.[74] As far as the Ru 3d core levels are concerned, overlapping between C 1s and Ru 3d$_{3/2}$ or satellite peaks makes the analysis more complex (Fig. 5C). Nonetheless, deconvolution analysis yielded two well-defined emission lines at 280.45 and 284.60 eV assigned to Ru 3d$_{5/2}$ and Ru 3d$_{3/2}$ which are typical of the Ru^{4+} oxidation state of Ru which confirmed that RuO$_2$ nanoparticles were actually formed.[48] Moreover, the deconvolution of the XPS spectrum revealed an additional feature with broader line width at 281.9 eV for the Ru 3d$_{5/2}$ line higher than the major peak by 1.45 eV. Also detected on oxidized ruthenium metal surfaces, the exact origin of this satellite peak still remains under debate since it has been assigned to excitation of the RuO$_2$ plasmon,[75] the surface species of Ru high bonding states,[76] or to a final-state screening effect.[77] Finally, analysis of the asymmetric O 1s emission line of the 4 wt% RuO$_2$/ZnO sample gave three signals at 529.03, 530.70, and 531.84 eV which were attributed to the lattice oxygen in RuO$_2$, lattice oxygen in ZnO[78] and oxygen of surface hydroxyl group of RuO$_2$ and ZnO,[79] respectively. As a result, XPS data further confirmed that the RuO$_2$/ZnO nanocomposites actually include RuO$_2$ and ZnO along with surface hydroxyl groups. The presence of the latter is fully consistent with FTIR data, these groups being expected to play an important role in the photocatalytic property of semiconductor by capturing photoinduced holes to produce hydroxyl radical, leading to better photocatalytic property.[80]

To get an in depth view of the interface properties of RuO$_2$/ZnO heterojunction, the contact properties including the spectroscopically accessible band bending developed at the interface between RuO$_2$ and ZnO particles was determined by XPS and by ultraviolet photoelectron spectroscopy (UPS) from the core level binding energy shifts. These results have to be compared to interface studies as obtained from in situ built-up heterointerfaces by depositing RuO$_2$ onto ZnO substrates, which will provide a detailed insight into the contact formation process (see below). First of all, the evolution of the core level spectra of RuO$_2$/ZnO nanocomposites was followed by increasing the RuO$_2$ amount (Fig. 6A-C). As shown in Fig. 6A, the Zn 2p$_{3/2}$ line shape did not change with increasing the RuO$_2$ content whereas the intensity of the Ru 3d$_{5/2}$ emission line increased gradually (Fig. 6C). Furthermore, both Zn 2p$_{3/2}$ and O 1s peaks were clearly shifted to lower binding energies with the increasing RuO$_2$ content. According to the difference between the core level energy values measured for pure ZnO and 6 wt% RuO$_2$/ZnO nanocomposite, the Zn 2p$_{3/2}$ and O 1s peaks were shifted to lower binding energies by 0.40 ± 0.05 and 0.45 ± 0.05 eV, respectively, from their original values. The slightly higher shift observed from O 1s peak than Zn 2p$_{3/2}$ peak might be due to contribution from both ZnO and RuO$_2$. In the following, we consider a rather parallel shift of both Zn 2p$_{3/2}$ and O 1s emission lines ignoring

this slight difference in peak shift. The Ru $3d_{5/2}$ emission line was also shifted to lower binding energy by an amount of 0.25 ± 0.05 eV and changes its spectral shape from a rather broad emission line at higher binding energy to a sharp line followed by a shake-

5 up satellite due to free electron excitation as typically found for metallic transition metal compounds which is due to bulk RuO_2. In addition, the work function of ZnO was determined by UPS. Thus according to the secondary electron cutoff recorded with UPS using HeI (Fig. 6D), the work function for pure ZnO was

10 estimated to be about 4.2 eV. This value is in good agreement with the work function reported in the literature for n-type ZnO.[81] Finally, XPS spectra indicated that the valence band maximum (VBM) of ZnO shifted toward lower binding energy with increasing RuO_2 content (Fig. 6E).

15 More quantitatively, the VBM values, deduced by linearly extrapolating the low binding energy edge of the valence band intersecting with the background, were found to be 2.90 ± 0.05, 2.75 ± 0.05, 2.60 ± 0.05 and 2.5 ± 0.05 eV for ZnO, 2 wt% RuO_2/ZnO, 4 wt% RuO_2/ZnO and 6 wt% RuO_2/ZnO,

20 respectively. These values suggested that as-synthesized ZnO is a n-type semiconductor. The evident shift of the VBM was 0.4 ± 0.05 eV, which is consistent with the shifts observed in Zn $2p_{3/2}$ and O 1s core levels shown above. These shifts can be related to a minimum band bending of ZnO at the interface. If these data are

25 used without any further consideration of the specific measurement conditions an energy band diagram of RuO_2/ZnO heterojunction showing the band bending at the interface between RuO_2 and ZnO may be proposed (Fig. S5). However, the above given deduction of the band energy diagram as deduced from the

30 photoelectron spectral data does not consider the specific 3D nano-structure of the photocatalysts and surface sensitivity of XPS which tells us that the energy diagram shown in Fig. S5 has to be handled with care, which is immediately evident if we compare the data obtained from the photocatalysts to the in situ

35 formed heterointerface. The XPS data obtained during a step-by-step sputter deposition of RuO_2 on ZnO single crystalline surfaces (0001) and (000$\bar{1}$) compared to a polycrystalline surface is shown in Fig. 7. Qualitatively the spectra are in good accordance to each other and also to the XP spectra shown above

40 for the photocatalysts indicating the quality of the wet chemical processing route. However as revealed by the attenuation of the ZnO substrate lines in the layer-by layer formed heterointerface already a RuO_2 thickness of 1 nm leads to a dominance of the RuO_2 overlayer in the XP spectra. In addition, the space charge

45 width W related to the complete formation of the band bending ΔV depends on the doping density N_D according to $W = (2\varepsilon\,\varepsilon_0\,\Delta V/\,e^2\,N_D)^{1/2}$ and may be expected to be at least above 100 nm for doping densities of 10^{18} cm^{-3} (E_{CB}-E_F about 0.3 eV is deduced from the valence band spectra of the samples). As a consequence

50 the ZnO spectral contributions of the 3D composites are dominated by the uncovered ZnO areas, whereas the RuO_2 covered areas showing full band bending hardly contribute to the spectra due to overlayer attenuation. In addition, the full space charge layer needs sample thicknesses beyond 100 nm to fully

55 develop.

Furthermore, the surface potential values depends on the orientation of the substrate as is also presented in Fig. 7 showing the difference between the valence band maximum of
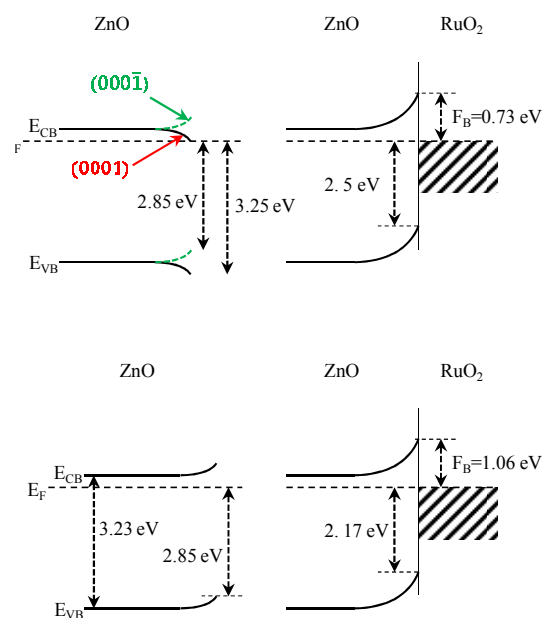

60 **Fig. 8** (top, left) Energy band diagrams for clean ZnO(0001) and ZnO(000$\bar{1}$) surfaces showing the difference in valence band maxima. (top, right) Energy band diagram of the ZnO/RuO_2 interfaces as determined from stepwise deposition of RuO_2. The resulting Schottky barrier is the same for both surface orientations. (bottom, left) Energy

65 band diagrams for clean polycrystalline ZnO surfaces (bottom, right) Energy band diagram of the polycrystalline ZnO/RuO_2 interfaces as determined from stepwise deposition of RuO_2.

ZnO(0001) and ZnO(000$\bar{1}$) surfaces which may be compared to the value obtained for the polycrystalline in situ prepared ZnO

70 surface also shown. These evident differences in the valence band maxima indicate the influence of different electronic DOS distributions of surface defects formed on different ZnO surfaces which also depends on the specific surface treatment. As a consequence the Schottky band bending of ZnO/RuO_2

75 heterointerfaces will differ to each other as shown in Fig. 8 in a variation of values between 0.4 and 0.8 eV. In any case a ZnO photocatalyst particle with approximate spherical shape will provide different surface states and therefore different valence band maxima at different surface facets and thus also different

80 band bending values for different surface orientations. Finally, Fig. 6E and 8 confirm the submetallic character of RuO_2 particles since the VB edge maximum states consisting of filled Ru 4d states (partially mixed with the O 2p state) extends to about 0 eV of binding energy, which is equivalent to the Fermi level E_F. As a

85 consequence, this character confers very interesting properties for energy applications on the samples prepared since it gives rise to a strong intraband optical absorption and high charge carrier density and conductivity in comparison to other stoichiometric metal oxides.

90 ### 3.3 Photocatalytic activity

The photocatalytic performance, stability and recyclability of the RuO_2/ZnO samples were evaluated by photodegradation under UV illumination of methylene blue (MB) and methyl orange (MO) which are, respectively, typical cationic and anionic

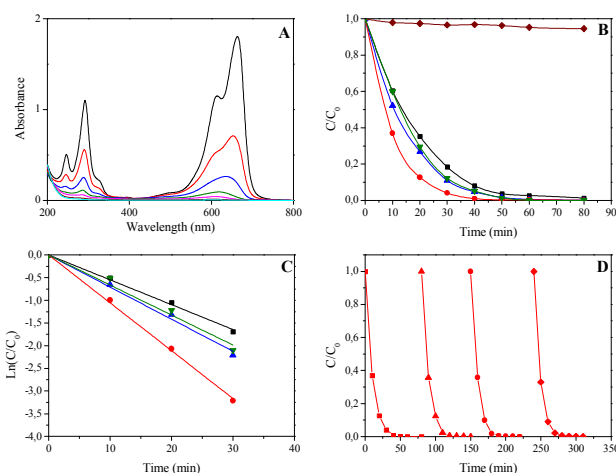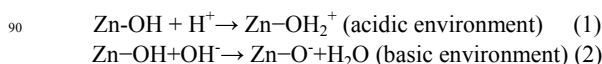95 organic water pollutants.[82] For sake of comparison, the respective

Fig. 9 (A) Absorbance changes of MB solution after different irradiation times in the presence of the 4wt% RuO_2/ZnO sample: equilibrium (black), 10 min (red), 20 min (blue), 30 min (olive), 40 min (magenta), 50 min (wine) and 60 min (cyan). (B) Kinetic of the degradation of MB in the presence of UV only (diamond, wine), ZnO (square, black), 2wt% RuO_2/ZnO (up triangle, blue), 4wt% RuO_2/ZnO (circle, red) and 6wt% RuO_2/ZnO (down triangle, olive) photocatalysts. (C) $ln[C/C_0]$ as a function of the irradiation time for ZnO (square, black), 2wt% RuO_2/ZnO (up triangle, blue), 4wt% RuO_2/ZnO (circle, red) and 6wt% RuO_2/ZnO (down triangle, olive) photocatalysts. (D) Cyclic runs in the photodegradation of MB using the 4wt% RuO_2/ZnO photocatalyst under UV-light: 1st cycle (square), 2[sd] cycle (triangle), 3rd cycle (circle) and 4th cycle (diamond).

activities of pure ZnO and commercial P25 TiO_2 were also investigated. Without any catalyst, MB and MO are quite stable molecules under UV illumination (Fig. 9 and S8) revealing that the photolysis mechanism can be ruled out. By contrast, a gradual decrease in absorption at 664 nm for MB and 464 nm for MO along with a slight shift of the bands to shorter wavelengths were observed upon addition of the nanocatalyst (Fig. 9A and S5A). Regardless of the nature of the dye studied, all RuO_2/ZnO heterosructures studied exhibited an enhanced photocatalytic activity compared to that of pure ZnO. Thus, after 20 min of UV-light illumination, the photodecomposition efficiency of MB was about 65%, 73%, 88% and 71% for pure ZnO, 2wt% RuO_2/ZnO, 4wt% RuO_2/ZnO and 6 wt% RuO_2/TiO_2. As a consequence, the optimum RuO_2 amount appeared to be 4 wt%, 4wt% RuO_2/ZnO heterostructure showing an efficiency even slightly higher than P25 TiO_2. Moreover, a same trend has been observed in the photodegradation of MO (Fig. S8).

To get further and more quantitative insights in the photocatalytic activities of the RuO_2/ZnO heterostructures, the kinetic analysis of the MB and MO degradation was achieved. The photodegradation of MB and MO by RuO_2/ZnO heterostructures followed a first- order law, $ln(C/C_0) = - k_{app}t$, where k_{app} is the pseudo fisrt-order rate constant (Fig. 9C and S5C, Table 1). Whatever the RuO_2 content, the reaction rates of the RuO_2/ZnO nanocomposites were much higher than that of pure ZnO. In particular, 4wt% RuO_2/ZnO led to the highest photocatalytic activities with rate constants of 0.106 and 0.035 min^{-1} for MB and MO respectively, that was about two times higher than those of pure ZnO (0.054 and 0.024 min^{-1} for MB and MO respectively) and comparable to those of commercial P25

TiO_2 (0.101 and 0.033 min^{-1} for MB and MO respectively). Although the surface areas of the RuO_2/ZnO heterostructures (i.e. 22-29 $m^2.g^{-1}$) were lower than those of pure ZnO (i.e. 31 $m^2.g^{-1}$) and commercial P25 TiO_2 (i.e. 47 $m^2.g^{-1}$), the photodecomposition rates measured for the nanocomposites were much higher than that of pure ZnO and close to this of commercial P25 TiO_2 that clearly evidences the synergistic interaction between RuO_2 and ZnO nanoparticles related to the favorable band alignment structure. On the other hand, it has been well-established that ZnO generally suffers from photocorrosion during photocatalytic processes.[83,84,85] Hence it is of prime importance to probe the photostability of the RuO_2/ZnO heterostructures. In this aim, combined cyclic photodegradation experiments and XRD studies were carried out. No noticeable change in the photocatalytic activity was detected even though the photocatalyst went through four successive recycles. Moreover, XRD patterns of the used and fresh samples revealed intact crystalline phase of the RuO_2/ZnO heterostructure after successive uses (Fig. S9). These results clearly evidence the stability of the RuO_2/ZnO heterostructures during the course of photodegradation processes.

Another key factor ruling the photocatalytic activities of semiconducting materials is the pH value of the solution. Indeed, organic compounds in wastewater greatly differ in several parameters, particularly in their speciation behavior, solubility in water and hydrophobicity. While some compounds are uncharged at common pH conditions typical of natural water or wastewater, other compounds exhibit a wide variation in speciation (or charge) and physico-chemical properties. At pH lower than pK_a, an organic compound exists as a neutral species whereas above pK_a, organic compound reaches a negative charge. In some cases, some compounds can exist in positive, neutral, as well as negative forms in aqueous solution. On the other hand, pH also determines the surface charge of the photocatalyst and the size of aggregates it forms. As a result, the solution pH deeply affects the surface charge of photocatalyst and ionization and/or speciation organic pollutants that could have important consequences on the adsorption and photocatalytic oxidation of organic pollutants. Primarily, in aqueous medium, hydroxylation of ZnO particles can take place leading to hydroxide layers (Zn-OH).[86] The zinc hydroxide surface (Zn-OH) can become charged by reacting with H^+ (acidic environment) or OH^- (basic environment) ions due to surface amphoteric reactions (Eq. 1, 2).[87]

$$Zn\text{-}OH + H^+ \rightarrow Zn\text{−}OH_2^+ \text{ (acidic environment)} \quad (1)$$
$$Zn\text{−}OH + OH^- \rightarrow Zn\text{−}O^- + H_2O \text{ (basic environment)} \quad (2)$$

The zero point of charge of ZnO (pH_{zpc}) has been reported to be 7.5-9.8.[88,89] Therefore, the surface functional groups of ZnO can be $ZnOH_2^+$, ZnOH, and ZnO^- at pH < pH_{zpc}, pH_{zpc} and pH > pH_{zpc}, respectively. On the other hand, MB dye ($pKa \approx 3.8$) at high pH (pH ≥ pKa), exists as a cation in aqueous solution. The effect of pH on the efficiency of photocatalytic degradation of MB was examined at the pH = 2.5, 7.5 and 9.9 (Fig. S10). After 20 min irradiation, the percentages of MB degradation were 87, 79 and 60% at pH 9.9, 7.5 and 2.5, respectively. The enhanced photodegradation of MB at higher pH was attributed to the favorable adsorption of the cationic MB dye on the negatively
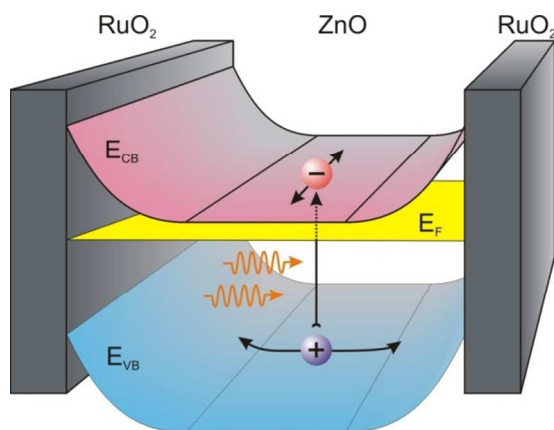
Fig. 10 3D draft of a hypothetical band energy space charge distribution as to be expected for a ZnO nano particle with RuO$_2$ co-catalysts deposited on opposite sides. As a consequence the light induced electron-hole pairs will be separated into different directions as indicated by the influence of an inhomogeneous potential or electric field distribution.
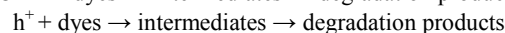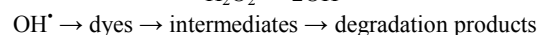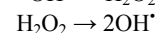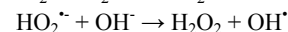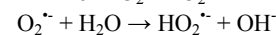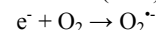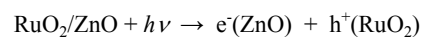
charged oxide surface. On the other hand, at lower pH the electrostatic repulsion between the MB cations and positively charged oxide surface greatly reduces the adsorption of the MB dye resulting in a drastic decrease in degradation rate. It has also been reported that in a slightly alkaline solution (pH 8-9), hydroxyl radicals are more easily generated by oxidizing the available OH$^-$ on the photocatalyst surface.[90,91] Thus, generally, the photodegradation efficiency is expected to be enhanced with increasing pH due to the ready availability of hydroxyl radicals for the reaction.

3.4 Mechanistic considerations

The enhanced photocatalytic activity of RuO$_2$/ZnO nanocomposites can be related to the role of RuO$_2$ on the surface of ZnO nanoparticles. Combining the morphology of RuO$_2$/ZnO nanocomposites and the interface analysis data reported above, it is clear that the electronic structure including the surface potentials of a 3D photocatalyst is rather complicated and cannot be described by one mean value of the valence band positions, the band bending and the work function, but must be considered (depending on the crystalline quality) as a 3D arrangement of different semiconductor junctions in different orientations depending on the given facets and possibly formed metal contacts on top of these. Considering as a probable example the formation of RuO$_2$ deposits on two opposing sides of a ZnO nanoparticle (the typical size of which being about 25-30 nm according to TEM studies) its electronic properties may be best described by the schematic representation shown in Fig. 10. In this case a strong band bending is formed just below the RuO$_2$ contact phase. Other areas of the ZnO cluster may remain mostly free of co-catalyst and will only form part of the expected space charge layer due to size restrictions. Illumination of such heterostructure RuO$_2$/ZnO nanocomposites will lead to the flow of holes to the RuO$_2$ co-catalyst contact layer and subsequent charge transfer reactions, whereas the electrons will flow to bare areas on the particle and react from there. This directional difference in electron and hole flow results from the inhomogeneous

distribution of the electric field in the non-homogeneously covered RuO$_2$/ZnO nano-composites. The electric field distribution is directly related to the gradient of the space charge or band bending potential (E= - grad ϕ_{bb}) as indicated in the distribution of the space charge layer in Fig. 10. We expect that similar conditions may be formed for many composite particles where semiconductor particles are modified with metallic co-catalysts. It is also clear from this representation that a preferential design of such composite particles needs an inhomogeneous co-catalyst distribution in order to disturb the spherical electronic structure of the photocatalysts and to enhance a vectorial charge separation of electron-hole pairs by inhomogeneous space charge layers.

This efficient charge separation can also increase the lifetime of the charge carriers and enhance the efficiency of the interfacial charge transfer to adsorbed substrates, and thus accounting for the higher activity of the RuO$_2$/ZnO nanocomposites. The photocatalytic reaction process can be proposed as follows

$$RuO_2/ZnO + h\nu \rightarrow e^-(ZnO) + h^+(RuO_2)$$
$$e^- + O_2 \rightarrow O_2^{\bullet-}$$
$$O_2^{\bullet-} + H_2O \rightarrow HO_2^{\bullet-} + OH^-$$
$$HO_2^{\bullet-} + OH^- \rightarrow H_2O_2 + OH^{\bullet}$$
$$H_2O_2 \rightarrow 2OH^{\bullet}$$
$$OH^{\bullet} \rightarrow dyes \rightarrow intermediates \rightarrow degradation\ products$$
$$h^+ + dyes \rightarrow intermediates \rightarrow degradation\ products$$

The electrons in the conduction band of ZnO can react with molecular oxygen adsorbed on the surface of ZnO to generate superoxide radials anion (O$_2^{\bullet-}$). The O$_2^{\bullet-}$ radicals further react with H$_2$O to produce OH$^{\bullet}$ radicals. On the other hand, holes migrated to RuO$_2$ react with surface-bound hydroxyl groups (or H$_2$O) to produce activated hydroxyl species (OH*) which is an extremely strong oxidant for the mineralization of organic substrates as dyes (MB or MO). In addition, photogenerated holes transferred to RuO$_2$ surface can also directly oxidize the organic dyes through the formation of intermediates.

Conclusion

Heterostrucrure RuO$_2$/ZnO nanomaterials were successfully prepared by a two-step procedure involving the synthesis of ZnO nanoparticles by the homogeneous precipitation method followed by further impregnation of wurtzite ZnO nanoparticles in an aqueous ruthenium (III) chloride hydrate and, then, thermally annealed at 350 ºC. UV-vis diffuse reflectance studies showed that the band gap energy of the RuO$_2$/ZnO heterojunction photocatalysts was slightly red-shifted compared to that of pure ZnO$_2$, with enhanced light absorption in the visible region due to surface plasmon resonance. An energy band diagram of RuO$_2$/ZnO nanocomposites was also determined by XPS and UPS from the shift of Zn 2p$_{3/2}$ and O 1s core level spectra. A shift of Zn 2p$_{3/2}$ and O 1s core level spectra were determined to be at least 0.40 ± 0.05 and 0.45 ± 0.05 eV, respectively, which was ascribed to inhomogeneous band bending effects due to heterojunctions formed on the RuO$_2$/ZnO nanoparticles. The latter photocatalysts showed higher photocatalytic activity than pure ZnO for the degradation of MB and MO dyes under UV light irradiation, in neutral and basic media, due to improved

separation of photogenerated electrons and holes resulting from the internal electric field. Moreover, the inhomogeneous RuO_2 distribution over ZnO nanocrystallites disturbs the spherical electronic structure of the photocatalysts and, as a consequence,
5 leads to a vectorial charge separation of electron-hole pairs into different directions. Furthermore, the RuO_2/ZnO nanocomposites could be easily recycled as heterojunction photocatalyst without decrease of photocatalytic activity confirming the stability of the as-synthesized RuO_2/ZnO photocatalysts. We expect that similar
10 effects are also operative in most photocatalysts reported in literature after modification with contact phases such as RuO_2/TiO_2 heterointerfaces.[47] The improved efficiency of the contact phase for enhancing the photocatalytic efficiency by improved charge carrier separation is clearly related to a defined
15 inhomogeneity in the contact phase distribution around the semiconductor particle. Only in cases where the electric potential distribution equivalent to an inhomogeneous distribution of the electric field induces the drift of electrons and holes into different directions the quantum efficiency of the photocatalytic reactions
20 can be expected to be strongly increased. In the ideal case a Janus type heterojunction arrangement seems to be most efficient device arrangement. This concept of semiconducting heterojunction nanocatalysts with high photocatalytic activity should be extended to other reactions as e. g. hydrogen
25 production. Experiments on this topic are currently in progress in our group.

Acknowledgements

Notes and references

[a] *Institut des Sciences Moléculaires, ISM UMR 5255 CNRS Groupe Matériaux, Université de Bordeaux, 33405 Talence Cédex, France. Fax:*
40 *+ 33 5 40006994; Tel: + 33 5 40002523; E-mail: t.toupance@ism.u-bordeaux1.fr*
[b] *Institute of Material Science, Technische Universität Darmstadt, Petersenstr. 23, 64287 Darmstadt, Germany.*

45 † Electronic Supplementary Information (ESI) available: FTIR spectra, EDX analysis, N_2 sorption data. Complementary interface analysis and photocatalytic data (MB adsorption in the dark, MO decomposition and effect of the pH), XRD patterns of the RuO_2-ZnO nanocatalyst after photocatalysis. See DOI: 10.1039/b000000x/

1 M. R. Hoffmann, S. T. Martin, W. Choi and D. W. Bahnemann, *Chem. Rev.,* 1995, **95**, 69.
2 D. Ravelli, Dondi, M. Fagnoni and A. Albini, *Chem. Soc. Rev.,* 2009, **38**, 1999.
3 C. Yu, G. Li, S. Kumar, K.Yang and R. Jin, *Adv. Mater.,* 2014, **26**, 892.
4 A. Kubacka, M. Fernandez-Garcia and G. Colon, *Chem. Rev.,* 2012, **112**, 1555.
5 N. Roy, Y. Sohn and D. Pradhan, *ACS Nano,* 2013, **7**, 2532.
6 Q. Zhang, C. S. Dandeneau, X. Zhou and G. Cao, *Adv. Mater.,* 2009, **21**, 4087.
7 L. Lan, L. Liu, R. Li, Z. Leng and S. Gan, *Ind. Eng. Chem. Res.,* 2014, **53**, 3131.
8 K. Kakiuchi, E. Hosono and S. Fujihara, *J. Photochem.Photobiol. A,* 2006, **179**, 81.
9 T. R.Zhang, W. J. Dong, M. Keeter-Brewer, S. Konar, R. N. Njabon and Z. R. Tian, *J. Am. Chem. Soc.,* 2006, **128**, 10960.
10 A. A. Khodja, T. Sehili, J. F. Pilichowski and P. Boule, *J. Photochem.Photobiol. A,* 2001, **141**, 231.
11 N. Daneshvar, D. Salari and A. R. Khataee, *J. Photochem. Photobiol. A,* 2004, **162**, 317.
12 C. A. K. Gouvea, F. Wypych, S. G. Moraes, N. Duran, N. Nagata and P. Peralta-Zamora, *Chemosphere,* 2000, **40**, 433.
13 B. Dindar and S. Icli, *J. Photochem. Photobiol. A,* 2001, **140**, 263.
14 Y. J. He, X. Y. Yu, T. L. Li, L. Y. Yan and B. L. Yang, *Powder Technol.,* 2006, **166**, 72.
15 C. Kim, S. J. Doha, S. G. Leea, S. J. Leea and H. Y. Kima, *Appl. Catal. A,* 2007, **330**, 127.
16 C. Wang, X. M. Wang, B. Q. Xu, J. C. Zhao, B. X. Mai, P. A. Peng, G. Y. Sheng and J. M. Fu, *J. Photochem. Photobiol. A,* 2004, **168**, 47.
17 M. L. Zhang, T. C. An, X. H. Hu, C. Wang, G. Y. Sheng and J. M. Fu, *Appl. Catal. A,* 2004, **260**, 215.
18 G. Marci, A. Augugliaro, M. J. Lopez-Munoz, C. Martin, L. Palmisano, V. Rives, M. Schiavello, R. J. D. Tilley and A. M. Venezia, *J. Phys. Chem. B,* 2001, **105**, 1033.
19 W. L. Kostedt, A. A. Ismail and D. W. Mazyck, *Ind. Eng. Chem. Res.,* 2008, **47,** 1483.
20 M. Agrawal, S. Gupta, A. Pich, N. E. Zafeiropoulos and M. Stamm, *Chem. Mater.,* 2009, **21**, 5343.
21 S. Yuan, J. Mu, R. Mao, Y. Li, Q. Zhang and H. Wang, *ACS Appl. Mater. Interfaces,* 2014, **6**, 5719;
22 W. Cun, Z. Jincai, W. Xinming, M. Bixian, S. Guoying, P. Ping'an and F. Jiamo, *Appl. Cat. B,* 2002, **39**, 269.
23 Z. Wen, G. Wang, W. Lu, Q. Wang, Q. Zhang and J. Li, *Cryst. Growth Des.,* 2007, **7**, 172.
24 W.-W. Wang, Y.-J. Zhu and L.-X. Yang, *Adv. Funct. Mater.,* 2007, **17**, 59.
25 L. Zheng, Y. Zheng, C. Chen, Y. Zhan, X. Lin, Q. Zheng, K. Wie and J. Zhu, *Inorg. Chem.,* 2009, **48**, 1819.
26 Z. Zhang, C. Shao, X. Li, L. Zhang, H. Xue, C.Wang and Y. Liu, *J. Phys. Chem. C*, 2010, **114** , 7920.
27 M. T. Uddin, Y. Nicolas, C. Olivier, T. Toupance, L. Servant, M. M. Müller, H. J. Kleebe, J. Ziegler and W. Jaegermann, *Inorg. Chem.,* 2012, **51**, 7764.
28 D. Li, H. Haneda, N. Ohashi, S. Hishita and Y. Yoshikawa, *Catal. Today,* 2004, **93-95**, 895.
29 D. Li and H. Haneda, *J. Photochem. Photobiol. A,* 2003, **160**, 203.
30 J. Lee, H. S. Shim, M. Lee, J. K. Song and D. Lee, *J. Phys. Chem. Lett.,* 2011, **2**, 2840.
31 P. Ray, S. P. Periasamy, C.-T. Liang and H.-T. Chang, *Environ. Sci. Technol.,* 2013, **47**, 6688.
32 W. He, H.-K. Kim, W. G. Wamer, D. Melka, J. H. Callahan and J.-J. Yin, *J. Am. Chem. Soc.,* 2014, **136**, 750.
33 J. Riga, C. T. Noel, J. J. Pireaux, R. Caudano and J. J. Verbist, *Phys. Scr.,* 1977, **16**, 351.
34 C. Sassoye, C. Laberty, H. Le Khanh, S. Cassaignon, C. Boissiere, M. Antonietti and C. Sanchez, *Adv. Funct. Mater.,* 2009, **19**, 1922.
35 C. Sassoye, G. Muller, D. P. Debecker, A. Karelovic, S. Cassaignon, C. Pizarro, P. Ruiz and C. Sanchez, *Green Chem.,* 2011, **13**, 3230.
36 K. M. Glassford and J. R. Chelikowsky, *Phys. Rev. B: Condens. Matter Mater. Phys.,* 1994, **49**, 7107.
37 A. J. Hartmann, M. Neilson, R. N. Lamb, K. Watanabe and J. F. Scott, *Appl. Phys. A: Mater. Sci. Process.,* 2000, **70**, 239.

38   A. Adeyemo, G. Hunter and P. K. Dutta , *Sens. Actuators B,* 2011, **152***,* 307.

39   Z. Mei, Y. Li, M. Fan, M. D. Argyle and J. Tang, *Int. J. Hydrogen Ener*gy, 2014, **39**, 14808.

40   C. Mondelli, A. P. Amrute, F. Krumeich, T. Schmidt and J. Pérez-Ramirez, *ChemCatChem,* 2011, **3**, 657.

41   J. Pérez-Ramírez, C. Mondelli, T. Schmidt, O. F.-K. Schlüter, A. Wolf, L. Mleczko and T. Dreier, *Energy Environ. Sci.,* 2011, **4**, 4786.

42   Y. Inoue, *Energy Environ. Sci.,* 2009, **2**, 364.

43   T. Sakata, K. Hashimoto and T. Kawai, *J. Phys. Chem.,* 1984, **88**, 5214.

44   A. P. Seitsonen and H. Over, *J. Phys. Chem. C,* 2010, **114**, 22624.

45   A. A. Ismail, L. Robben and D. W. Bahnemann, *ChemPhysChem,* 2011, **12**, 982.

46   S. Kundu, A. B. Vidal, F. Yang, P. J. Ramirez, D. D. Senanayake, D. Stacchiola, J. Evans, P. Liu and J. A. Rodriguez, *J. Phys. Chem. C,* 2012, **116**, 4767.

47   M. T. Uddin, Y. Nicolas, C. Olivier, T. Toupance, M. M. Müller, H. J. Kleebe, K. Rachut, J. Ziegler, A. Klein and W. Jaegermann, *J. Phys. Chem. C,* 2013, **117**, 22098.

48   R. Schafranek, J. Schaffner and A. Klein, *J. Eur. Ceram. Soc.*, 2010**, 30**, 187.

49   S. Bang, S. Lee, T. Park, Y. Ko, S. Shin, S.-Y. Yim, H. Seo and H. Jeon, *J. Mater. Chem.,* 2012, **22**, 14141.

50   T. Toupance, H. Elhamzaoui, B. Jousseaume, H. Riague, I. Sadeddin, G. Campet and J. Brötz, *Chem. Mater.*, 2006, **18***,* 6364.

51   S. Brunauer, P. H. Emmett and E. Teller, *J. Am. Chem. Soc.,* 1938, **60***,* 309.

52   V. Stengl and T. M. Grygar, *Int. J. Photoenergy,* 2011, *Article ID 685935, 1-13.*

53   F. Jahan, M. H. Islan and B. E. Smith, *Sol. Ener. Mater. Solar Cells,* 1995, **37**, 283.

54   E. Sanchez and T. Lopez, *Mater. Lett.,* 1995, **25**, 271.

55   O. Lang, A. Klein, C. Pettenkofer, W. Jaegermann and A. Chevy, *J. Appl. Phys.,* 1996, **80**, 3817.

56   R. Schlaf, O. Lang, C. Pettenkofer and W. Jaegermann, *J. Appl. Phys.,* 1999, **85**, 2732.

57   W. Mönch, in *Semiconductor surfaces and interfaces*, Springer-Verlag, Heidelberg, 1993.

58   Y. J. Kwon, K. H. Kim, C. S. Lim and K. B. Shim, *J. Ceram. Proc. Res.,* 2002, **3**, 146.

59   R. F. Silva and M. E. D. Zaniquelli, *Colliod. Surface A,* 2002, **198-200**, 551.

60   A. Umar, B. Karunagaran, E. K. Suh and Y. B. Hahn, *Nanotechnol.,* **2006**, *17*, 4072.

61   A. Khan and M. E. Kordesch, *Mater. Lett.,* 2008, **62**, 230.

62   A. J. Cheng, Y. Tzeng, H. Xu, S. Alur, Y. Wang, M. Park, T. H. Wu, C. L. Shannon, D. J. Kim and D. Wang, *J. Appl. Phys.,* 2009, **105***,* 073104.

63   T. C. Damen, S. P. S. Porto and B. Tell, *Phys. Rev.,* 1966, **144**, 570.

64   C. X. Xu, X. W. Sun, H. Zhang, L. Ke and S. J. Chua, *Nanotechnol.,* 2004, **15**, 856.

65   A. V. Korotcov, Y. S. Huang, K. K. Tiong and D. S. Tsai, *J. Raman Spectros.,* 2007, **38**, 737.

66   Y. S. Huang and P. C. Liao, *Sol. Energy Mater. Sol. Cells*, 1998, **55,** 179.

67   K. A. Alim, V. A. Fonoberov and A. A. Balandin, *J. Appl. Phys. Lett.,* 2005, **86***,* 053103.

68   M. Tzolov, N. Tzenov, D. D. Malinovska, C. Pizzuto, G. Vitali, G. Zollo and I. Ivanov, *Thin Solid Films,* 2000, **379**, 28.

69   G. J. Exarhos, A. Rose and C. F. Windish Jr., *Thin Solid Films,* 1997, **308**, 56.

70   M. Rajalakshmi and A. K. Arora, *J. Appl. Phys.,* 2000, **87**, 2445.

71   M. T. Colomer and J. R. Jurado, *Chem. Mater.*, 2000, **12**, 923.

72   J. Essick and R. Mather, *Am. J. Phys.,* 1993, **61**, 646.

73   R. Vinod, P. Sajan, S. R. Achary, C. M. Tomas, V. M. Sanjose and M. J. Bushiri, *J. Phys. D: Appl. Phys.,* 2012, **45**, 425103.

74   V. K. Dwivedi, P. Srivastava and G. V. Prakash, *J. Semicond.,* 2013, **34**, 033001.

75   H. Over, A. P. Seitsonen, E. Lundgren, M. Smedh and J. N. Andersen, *Surf. Sci.,* 2002, **504**, L196.

76   K. Reuter and M. Scheffler, *Surf. Sci.,* 2001, **490**, 20.

77   P. A. Cox, J. B. Goodenough, P. J. Travener, D. Telles and R. G. Egdell*, J. Solid State Chem.*, 1986, **62**, 360.

78   X. M. Teng, H. T. Fan, S. S. Pan, C. Ye and G. H. Li, *J. Appl. Phys.,* 2006, **100**, 053507.

79   S. Bai, T. Guo, D. Li, R. Luo, A. Chen and C. C. Liu, *Sens. Actuators, B,* 2013, **182**, 747.

80   A. L. Linsebigler, G. Lu and J. Y. Yates, *Chem. Rev.,* 1995, **95,** 735.

81   D. Kalblein, R. T. Weitz, H. J. Bottcher, F. Ante, U. Zschieschang, K. Kern and H. Klauk, *Nano Lett.,* 2011, **11**, 5309.

82   Y. Guo, H. Wang, C. He, L. Qiu and X. Cao, *Langmuir,* 2009, **25**, 4678.

83   P. Spatish and I. Poulios, *Corros. Sci.,* 1995, **37**, 673.

84   A. J. Hoffman, E. R. Carraway and M. R. Hoffmann, *Environ. Sci. Technol.,* 1994, **28**, 776.

85   A. V. Dijken, A. H. Janssen, M. H. P. Smitsmans, D. Vanmaekelbergh and A. Meijerink, *Chem. Mater.,* 1998, **10**, 3513.

86   S. Sakthivel, B. Neppolian, M. V. Shankar, B. Arabindoo, M. Palanichamy and V. Murugesan, *Solar Ener. Mater. Solar Cells,* 2003, **77,** 65.

87   A. Degen and M. Kosec, *J. Eur. Ceram. Soc.*, 2000, **20**, 667.

88   S. R. Rao and J. A. Finch, *Int. J. Miner. Process.,* 2003, **69**, 251.

89   S. Music, D. Dragcevic, M. Maljkovic and S. Popovic, *Mater. Chem. Phys.,* 2002, **77**, 521.

90   G. Shukla, *Appl. Phys. A: Mater. Sci. Process.,* 2009, **97**, 115.

91   G. Li, M. Zhu, J. Chen, Y. Li and X. Zhang, *J. Environ. Sci.,* 2011, **23**, 744.